SIMULATION OF DDT IN OBSTRUCTED CHANNELS: WAVY CHANNELS vs. FENCE-TYPE OBSTACLES

L. Nuti[1], J. Melguizo-Gavilanes[2,3]

[1]**Department of Industrial Engineering, University of Padua, 35122 Padova PD, Italy**

[2]**Institute Pprime, UPR 3346 CNRS, ISAE-ENSMA, 86961, Futuroscope-Chasseneuil, France**

[3]**Shell Global Solutions B.V., Energy Transition Campus, 1031 HW, Amsterdam, The Netherlands**

Abstract

The capabilities of an OpenFOAM solver to reproduce the transition of stoichiometric H_2-air mixtures to detonation in obstructed 2-D channels were tested. The process is challenging numerically as it involves the ignition of a flame kernel, its subsequent propagation and acceleration, interaction with obstacles, formation of shock waves ahead and detonation onset (DO). Two different obstacle configurations were considered in 10-mm high × 1-m long channels: (i) wavy walls (WW) that mimic the behavior of fence-type obstacles but prevent abrupt area changes. In this case, flame acceleration (FA) is strongly affected by shock-flame interactions, and DO often results from the compression of the gas present between the accelerating flame front and a converging section of the channel. (ii) Fence-type (FT) obstacles. In this case, FA is driven by the increase in flame surface area as a result of the interaction of the flame front with the unburned gas flow field ahead, particularly, downstream of obstacles; shock-flame interactions play a role at the later stages of FA, and DO takes place upon reflection of precursor shocks from obstacles. The effect of initial pressure, $p_0 = 25$, 50 and 100 kPa, at constant blockage ratio ($BR = 0.6$) was investigated and compared for both configurations. Results show that for the same initial pressure ($p_0 = 50$ kPa), the obstacle configurations could lead to different final propagation regimes: a *quasi-detonation* for WW, and a *choked-flame* for FT, due to the increased losses for the latter. At $p_0 = 25$ kPa however, while both configurations result in *choked flames*, WW seem to exhibit larger velocity deficits than FT due to longer flame-precursor shock distances during quasi-steady propagation and to the increased presence of unburnt mixture downstream of the tip of the flame that homogeneously explodes providing additional support to the propagation of the flame.

1. INTRODUCTION

The materialization of a hydrogen economy calls for practical and fundamental understanding of the risks associated with its production, storage and handling [1–3]. Accidental combustion events include phenomena such as ignition, flame propagation/acceleration, flame-obstacle interactions, shock formation, shock-flame interactions, transition-to-detonation, and detonation propagation. Among these, deflagration-to-detonation transition (DDT) as an outstanding problem in combustion science is the most fascinating.

Reacting flows in general, and DDT in particular, are challenging, both experimentally and numerically because of the wide range of spatial and temporal scales at which important physical and chemical

processes take place, oftentimes spanning over six orders of magnitude. Conventional methods relying on the discretization of the Reactive Navier-Stokes equations using finite differences/volumes [4] have proven to be effective, and very useful in unveiling the interplay between the chemical heat release and the gas dynamics in high-speed flows. However, their main limitation lies on the fact that the natural path towards tackling larger and more complex, industrially relevant problems is dependent on availability of/access to more computational power (i.e., large computing clusters); specialized mesh treatments such as static/adaptive mesh refinement [5, 6] and recycling meshes [7] are the exception in which the computational power variable is taken as constant and alternatives are sought to do more with less.

DDT is particularly expensive to compute because the physics at play during each stage of the process changes, and with it, the numerical methods/schemes that would allow for an efficient integration of these type of flows. While the initial stages are governed by diffusive processes, and the latter stages by shock compression, independently involving different physics, the dynamics of flame acceleration (FA) and detonation onset (DO) is highly dependent on the initial acceleration rates that rely on properly capturing the early development of intrinsic flame instabilities, as well as of hydrodynamic boundary layers [5]. Numerical schemes that perform well for a wide range of Mach numbers are thus needed.

This paper assesses the capabilities of an OpenFOAM solver [8] to reproduce DDT in partially obstructed narrow channels (i.e., characteristic lengths of the order of mm in which momentum losses to walls are expected to be large). The solver uses a hybrid implementation for the computation of numerical fluxes, following the developments of Kraposhin et al. [9], in which typical pressure-velocity coupling (i.e., Poisson solvers) are used for low flow velocities ($M \leq 0.3$), and flux-splitting together with appropriate flux limiting (i.e., central-upwind Kurganov-Tadmor scheme [10] with van Albada's limiter) to capture the flow discontinuities that arise in high-speed flows. This is an advantage over previous attempts for efficient simulation of DDT [11] in which the integration of FA required the use of two independent solvers.

The ultimate goal is to develop appropriate tools to reliably simulate the fully optically accessible smooth narrow channel built during the doctoral thesis of Ballossier [12], and carry out side-by-side comparisons with the novel experimental data previously/currently being collected in which the value of simultaneous schlieren visualization was demonstrated. Here however, as a first step in the solver validation process, two obstacle configurations are considered in 10-mm high × 1-m long channels: (i) wavy walls (WW) that mimic the behavior of fence-type obstacles but prevent abrupt area changes; seldom investigated [13, 14], and (ii) Fence-type (FT) obstacles; widely studied as a canonical configuration [15].

2. COMPUTATIONAL METHODOLOGY

2.1. Governing equations, transport and chemical model

The flow field in the channel was modeled using the reactive Navier Stokes equations (Eqns. (1)-(4)) with detailed chemistry and temperature dependent transport and thermodynamics (i.e., JANAF tables to compute species/mixture heat capacities, enthalpies and entropies) [16]. The Sutherland Law [17], modified Eucken relation [18] and JANAF polynomials [16] are used to account for the functional temperature dependence of mixture viscosity (μ), thermal conductivity (κ) and specific heat (c_p), respectively.

$$\partial_t \rho + \nabla \cdot (\rho \mathbf{u}) = 0 \quad \text{(Mass)} \tag{1}$$

$$\partial_t(\rho \mathbf{u}) + \nabla \cdot (\rho \mathbf{uu}) = -\nabla p + \nabla \cdot \tau \quad \text{(Momentum)} \tag{2}$$

$$\partial_t(\rho Y_k) + \nabla \cdot (\rho \mathbf{u} Y_k) = -\nabla \cdot \mathbf{j_k} + \dot{\omega}_k \quad \text{(Species)} \tag{3}$$

$$\partial_t[\rho(h_s + K)] + \nabla \cdot [\rho \mathbf{u}(h_s + K)] = \frac{dp}{dt} - \nabla \cdot \mathbf{j_q} + \tau : \nabla \mathbf{u} + \dot{q}_{\text{chem}} \quad \text{(Energy)} \tag{4}$$

$$p = \rho \frac{R_u}{W_{\text{mix}}} T \tag{5}$$

with $K = \frac{1}{2}|\mathbf{u}|^2; \quad \tau = \mu(\nabla \mathbf{u} + \nabla \mathbf{u}^T) - \frac{2}{3}\mu(\nabla \cdot \mathbf{u})\mathbf{I}; \dot{q}_{\text{chem}} = \sum_{k=1}^{N} \Delta h_{f,i}^0 \dot{\omega}_k$

Where ρ is the density, $\mathbf{u}$ is the velocity, p is the pressure, h is the sensible enthalpy per unit volume, Y is the mass fraction of the k-th species, $\dot{\omega}_k$ is the reaction rate for the k-th species, τ is the viscous stress tensor, $\mathbf{j_k}$ is the species diffusion flux, $\mathbf{j_q}$ is the heat flux, $\dot{q}_{\text{chem}}$ is the rate of conversion of chemical into thermal energy, $\Delta h_{f,i}^0$ is the enthalpy of formation of species, R_u is the specific gas constant, μ is the mixture viscosity. The species diffusion term, $\mathbf{j_k}$, uses Fick's law for binary mixtures. For multicomponent mixtures where one component is present in large amounts (i.e., N_2 for combustion in air) all other species may be treated as trace species. Writing the binary diffusion coefficient with respect to N_2 only yields:

$$\mathbf{j_k} = -\rho D_k \nabla Y_k \tag{6}$$

where D_k is the effective diffusion coefficient. In Eq. 6, thermodiffusion or Soret effect has been neglected. The mass conservation equation, Eq. 3, and only $N - 1$ species equations are solved for. The last species mass fraction, N_2, is obtained by writing $Y_{N_2} = 1 - \sum_{k=1}^{N-1} Y_k$ and absorbs all inconsistencies introduced by Fick's law. This error is negligible when the last species, Y_{N_2}, is at a high concentration as is the case for combustion in air [4]. The heat flux $\mathbf{j_q}$ includes the effect of sensible enthalpy transport by diffusion

$$\mathbf{j_q} = -\frac{\kappa}{c_p}\nabla h_s + \sum_{k=1}^{N-1} h_{s,k}\left(\mathbf{j_k} - \frac{\kappa}{c_p}\nabla Y_k\right) = -\frac{\kappa}{c_p}\nabla h_s + \sum_{k=1}^{N-1} h_{s,k}\left(1 - \frac{1}{Le_k}\right)\frac{\kappa}{c_p}\nabla Y_k \tag{7}$$

In Eq. 7, $Le_k = \kappa/(c_p \rho D_k)$ is the Lewis number per species k. Le_k is assumed to be unity, hence, the thermal diffusivity is used to model its mass diffusivity which simplifies Eq. 7 significantly. While the use of the latter assumption may be questionable for lean H_2 mixtures in which thermo-diffusive effects play an important role, it will be shown below to yield sensible results for stoichiometric H_2-air.

Equations (1)-(4) were solved in two-dimensional planar geometries (described in the next subsection) using the OpenFOAM Toolbox [8]; chemical kinetics was modeled with the 9-species, 21-reactions Mével's mechanism for hydrogen oxidation [19], whose ignition delay time and laminar burning predictions are in agreement with experimental data [20]. The spatial discretization of the solution domain is performed using finite volumes (FV) which allows for body-fitted hexagonal meshes that avoid the staircasing present when numerically integrating curved geometries with finite differences. The solver includes a hybrid implementation for the numerical fluxes that make it suitable for a wide range of Mach numbers; this is achieved by combining PISO methods (i.e. pressure-velocity coupling) in regions with low flow velocities ($M \leq 0.3$), together with standard techniques for high speed flows (i.e. flux-splitting and limiters). For the latter regime, the numerical fluxes at cell-faces are computed using a central-upwind Kurganov-Tadmor scheme [10, 21]. The flow variables on cell faces are reconstructed through

a second-order interpolation with a symmetric van Albada flux limiter which results in non-oscillatory bounded transitions across shocks and contact discontinuities. The chemical source terms are computed using a stiff ODE solver (i.e. fourth-order Rosenbrock). The PBiCGStab (Preconditioned Biconjugate Gradient Stabilized) method is used for all the linear systems resulting from the discretization of the governing equations, preconditioned through the DILU (Diagonal Incomplete-LU) technique. Finally, the time integration uses a second order Crank-Nicolson method, and the time step is dynamically adapted during the computation with an acoustic Courant number of 0.4 to ensure stability of the numerical scheme. Note that the solver capability to predict the global dynamics of detonation transmission in a curved chamber was recently tested and validated against experiments in [22]; this is the first time the solver is utilized in DDT scenarios.

2.2. Domain, initial and boundary conditions

The computational domains are shown in Fig. 1 (a) and (b) corresponding to channels with wavy and fence type obstacles, respectively, with blockage ratio, $BR = 0.6$. The latter is computed as $BR = 1 - h/H$ where h is the obstructed height, and H is the height of the channel.

a) Wavy walls (WW)

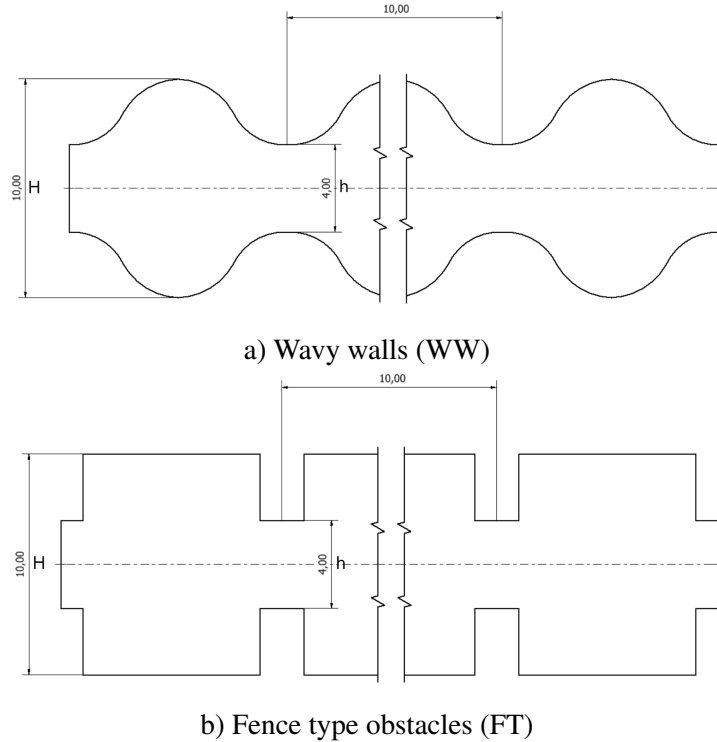
b) Fence type obstacles (FT)

Figure 1: Schematics of computational domains considered. The total length of the channel is 1-m, the values shown are given in mm.

Both geometries/computational grids were created using a blockMesh script so that in future different obstacle spacings, BR and channel lengths can be investigated. The $y-$coordinate of the top and bottom walls of the wavy channel obey the following relations:

$$y_{\text{top}} = aH \sin\left(\frac{x - cb\delta}{b\delta}2\pi\right) + H(1 - a); \quad y_{\text{bottom}} = aH \sin\left(\frac{x}{b\delta}2\pi\right) + aH \tag{8}$$

where a is the wave's amplitude, b its wavelength, and c denotes an offset of the top wall relative to the bottom wall to have the peaks/troughs of the waves in phase or out of phase; lengths are normalized by

the thermal flame thickness, δ. To reproduce the wavy channel used here, $a = 0.15$, $b = 1.25$, $c = 0.5$, and $\delta = 0.36$ mm, the latter kept fixed for all pressures hence the resolution changes quoted below.

Three initial pressures were considered $p_0 = 25$, 50 and 100 kPa to investigate the flame acceleration dynamics in the chamber as a function of increasing pressure. Initial conditions were quiescent mixture at $T_0 = 300$ K, and mass fractions $Y_{H_2} = 0.02851$, $Y_{O_2} = 0.22628$, $Y_{N_2} = 0.74521$, corresponding to a stoichiometric H_2-air mixture. Regarding boundary conditions, the channels are closed at the ignition end and open on the other end; a no-slip constraint for velocity, and zero gradient for temperature, species and pressure were imposed on the channel walls. Hexagonal uniform meshes were used; the number of cells in each direction was 7894 in x-direction and 78 in y-direction for a total of $615,732$ of cells in the entire domain. This corresponds to an approximately uniform mesh along the length and height of the channel of $\Delta x = \Delta y = 0.128$ mm. Given the chosen mesh size, there are $\sim$ 18 pts, 7 pts, 3 pts, per flame thickness, δ, for 25 kPa, 50 kPa and 100 kPa, respectively. In terms of the detonation induction length, l_{ind}, there are 5 pts, 2 pts and 1 pts as the initial pressure increases. Simulations were run using 20 processors, and took approximately 140 CPU hours per case. Finally, the flames were ignited by imposing three equally spaced hemi-spherical regions ($r = 1.2$ mm) of high pressure ($p_{ign}/p_0 = 5$) and temperature ($T_{ign}/T_0 = 6.6$) at the channel closed end. This initiation method resulted in the desired initially slow flames that subsequently accelerate and undergo a propagation regime change to achieve steady propagation. Table 1 lists properties such as the laminar burning velocity s_L, expansion ratio $\sigma = \rho_0/\rho_b$, thermal flame thickness ($\delta = (T_b - T_0)/(\nabla T)_{max}$), burnt products sound speed c_b, detonation induction length l_{ind}, and Chapman-Jouguet detonation velocity D_{CJ}, for all the mixtures tested. The reported values were computed using Cantera [23] and the Shock and Detonation Toolbox [24] with the detailed mechanism of Mével [19, 20]. For σ, a planar flame computation was performed to evaluate the burnt products density. Note that this approach yields slightly lower σ values (-0.05) than an equilibrium calculation at constant pressure and enthalpy.

Table 1: Combustion properties for stoichiometric H_2-air at different initial pressures and $T_0 = 300$ K.

Combustion properties	$p_0 = 25$ kPa	$p_0 = 50$ kPa	$p_0 = 100$ kPa
Laminar burning velocity, s_L	2.18 m/s	2.32 m/s	2.38 m/s
Expansion ratio, σ	6.71	6.77	6.81
Flame thickness, δ	2.31 mm	0.91 mm	0.36 mm
Burnt products sound speed, c_b	999.34 m/s	1002.93 m/s	1005.8 m/s
CJ speed, D_{CJ}	1936.93 m/s	1952.82 m/s	1967.84 m/s
Induction length, l_{ind}	0.56 mm	0.27 mm	0.14 mm

3. RESULTS AND DISCUSSION

3.1. $x - t$ and $u - x$ diagrams

The simulation results were postprocessed to extract $x - t$ and $u - x$ diagrams. To do so, the flame front position was tracked during the simulation. The *front* was defined as the location along the channel's centerline where the H radical peaked. This has been shown to be a better reaction zone marker than OH due to its short life time [22]. Figures 2 (a) and (b) show the results for the wavy walls, whereas Figs. 2 (c) and (d) show the evolution for the fence type obstacles. The $x - t$ diagrams for both configurations display a change of slope signaling a switch in propagation regime, and serve to pinpoint the exact location where the latter change takes place. The $u - x$ diagrams albeit noisy show the strong front acceleration typical of the process, and how initial pressure, p_0 affects the dynamics. As p_0 is decreased for a fixed

BR, the distance to reach a steady propagation regime increases, i.e., run-up distance, and the final front velocities attained decrease in line with the experimentally observed dependence [15].
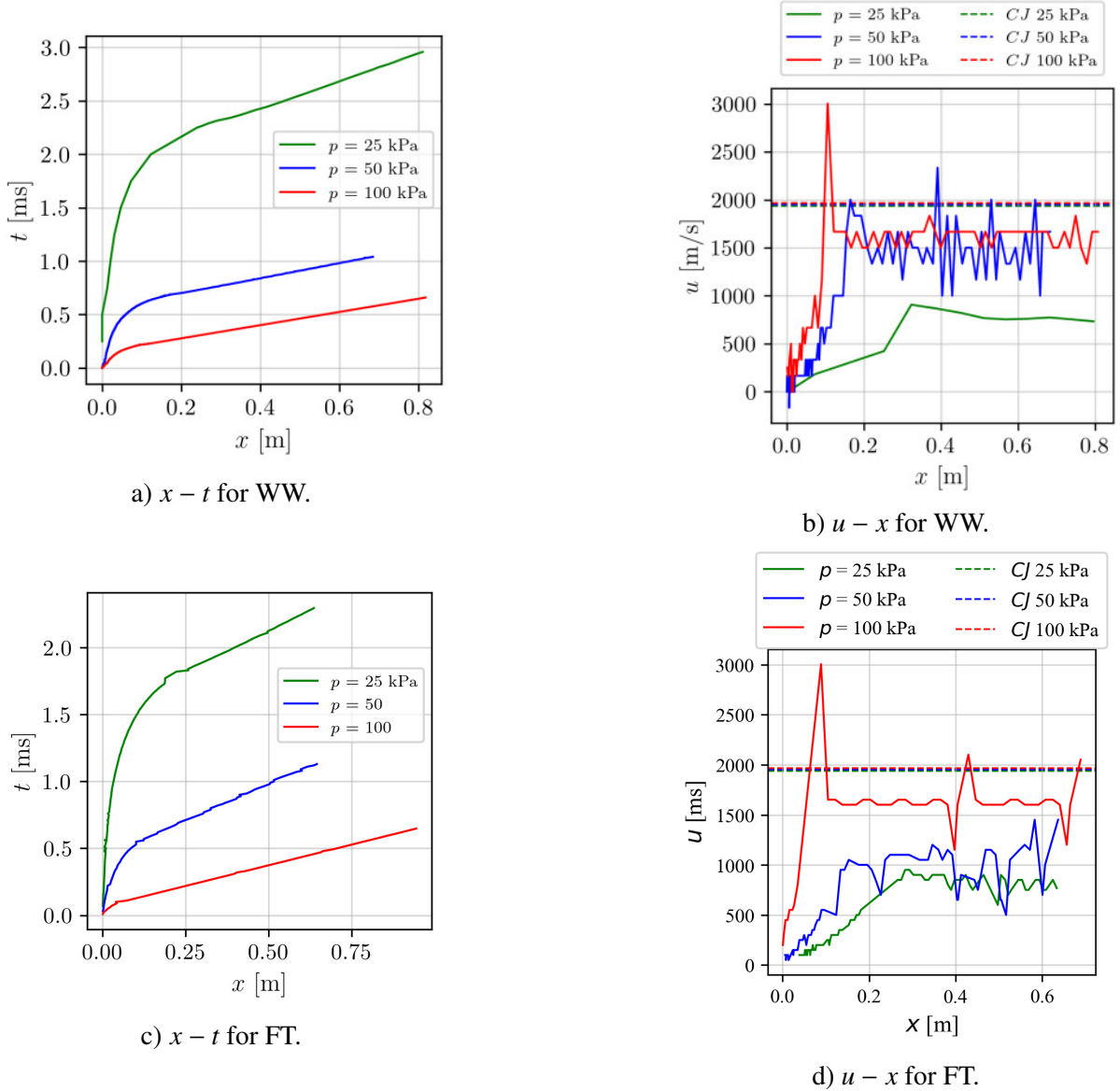

a) $x - t$ for WW.

b) $u - x$ for WW.

c) $x - t$ for FT.

d) $u - x$ for FT.

Figure 2: Left column: $x - t$ diagrams; front position, x, as a function of time, t. Right column: $u - x$ diagrams; front velocity, u, as a function of distance in the channel.

Figure 3 summarizes and compares the results obtained for all the initial pressures considered. Figure 3 (a) shows the run-up distance, x_{DDT}, evolution. The channel with wavy walls leads to larger x_{DDT} due to the smooth transition between obstacles which prevents strong shock reflections. The velocities attained during quasi-steady propagation, on the other hand (see Fig. 3 (b)), exhibit a rather unusual non-monotonic behavior. At the lowest and highest pressures tested the fence type obstacle configuration lead to higher velocities; the flow fields analyzed in the next section will shed some light on this outcome.

The propagation of fast combustion waves in obstacle laden channels can be classified as a function of the velocity deficit, u/D_{CJ}, at which their steady propagation is observed. The different regimes have been experimentally observed to be a function of the blockage ratio (at constant initial pressure,

p_0) or of the initial pressure (at constant blockage ratio, *BR*) [15]. Waves propagating in the range of $0.8 \leq u/D_{CJ} < 1.0$ are called *quasi-detonations* whereas those propagating at $u/D_{CJ} \sim 0.4 - 0.5$ are called *choked flames*. The latter regime is characterized by fast flames that trail a shock wave at distances significantly larger than in detonations, hence their propagation is not simply supported by adiabatic compression but diffusive processes are also argued to play a dominant role. A notable, non-trivial result from the present simulations is that at intermediate pressure ($p_0 = 50$ kPa; see table 2) the same initial conditions, i.e., mixture composition, initial temperature, and *BR*, lead to different propagation regimes, suggesting that their classification requires the specification of additional parameters. In the case at hand, whether the flame/shock-obstacle interactions are abrupt (FT) or smooth (WW).
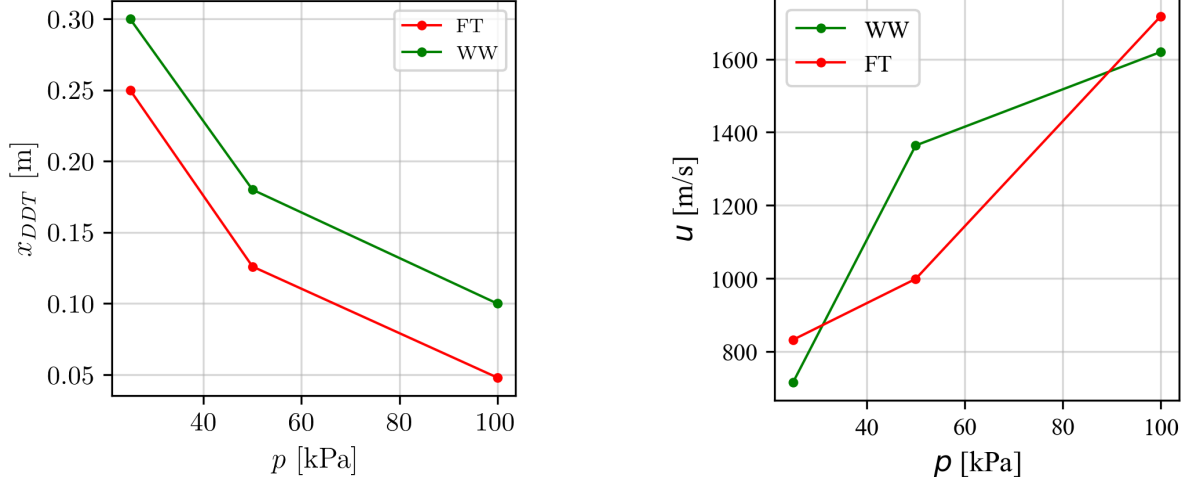

Figure 3: Results summary. Run-up distance, x_{DDT}, and front velocity during quasi-steady propagation, u, as a function of initial pressure, p, for the obstacle configurations considered.

Table 2: Quasi-steady propagation regimes for the obstacle configurations considered

p_0 [kPa]	Wavy walls	Fence type
100	Quasi-detonation	Quasi-detonation
50	Quasi-detonation	Choked flame
25	Choked flame	Choked flame

To enable a fair comparison between the geometries considered, given that x_{DDT} occurs at different locations along the channel length, in the section below the flow fields will be compared at the same propagation stage relative to x_{DDT}, i.e., $x/x_{DDT} \sim$ cte.

## 3.2. Propagation regimes changes for WW and FT at 50 kPa

3.2.1. Early/intermediate stages of FA

Upon ignition of the flame, the combustion process that drives the flame through the domain begins. The flow induced by the flame, and its interaction with the walls and obstacles causes an increase of the flame surface that in turn results in an increase of burning speed and flow velocity. The pressure increases/decreases at the converging/diverging sections for the wavy channel; for the fence-type obstacles, significant pressure increase takes place due to the earlier formation of shock waves ahead of the flame front. At 50 kPa, a marked increase in pockets of fresh mixture that are not completely burnt can be observed for FT, allowing for a larger flame surface and a higher reaction and preheat zone (orange
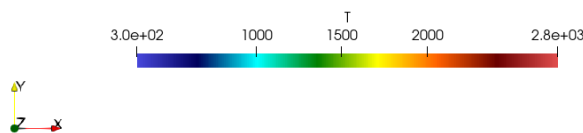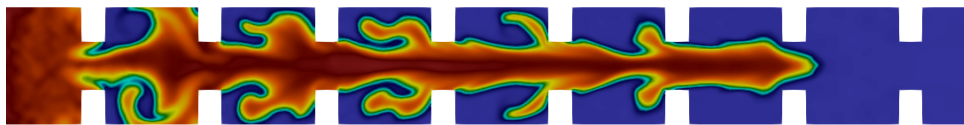
band and green band) in Fig. 4 where the evolution of the flame at $x/x_{DDT} \sim 0.5$ is depicted. For the FT domain, larger recirculation zones are present, and the flame does not advance as readily to consume the mixture along the height of the channel.

$$p_0 = 50 \text{ kPa}$$
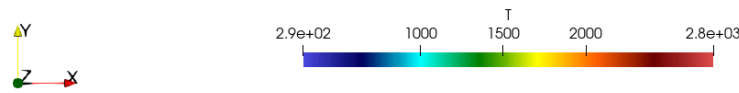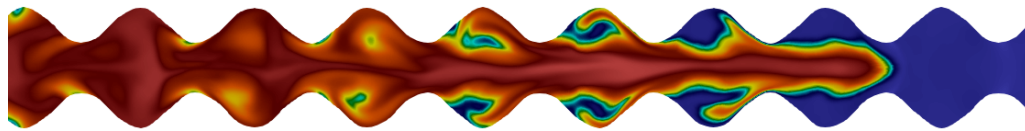
a) Wavy walls

b) Fence-type obstacles

Figure 4: Temperature fields at $x/x_{DDT} \sim 0.5$ for early stages of FA.

3.2.2. Late stages

The moment before a possible regime change is a very delicate condition and set of events that is dependent on several parameters; in this particular case, the initial pressure and obstacle type seemed to govern the dynamics. The shock waves formed at the flame front are reflected on the edges of the channel, bouncing from one wall to the other and also propagating opposite to the flame propagation direction. The thermal expansion induced flow in the unburned gases, lead to the formation of strong gradients in temperature and pressure. Pressure waves which propagate at the local speed of sound, coalesce, generating shock waves that impact against the fence-type obstacles or converging sections of the wavy channel, creating areas of very high temperature and pressure that could trigger a regime change (i.e., *quasi-detonation* or *choked flame*).

In the cases at hand, it is the interactions of the flame with the boundaries and precursor shock waves that result in a significant increase of the burning rate near the channel's walls. A few moments before the change in propagation regime sets in, the flame gets closer and closer to the precursor shock wave ahead

created by the acceleration of the flame itself. This feature causes the induction zone (green band), the reaction zone (orange band) and the combustion gases zone (red band) to become increasingly thinner, leading to the formation of an ignition center (not shown); see Fig. 5. As the flame velocity increases, the shock waves in front of the flame are approached, and these bands flatten out, thus shortening the time and space required for the reactions to take place.

A few features stand out in the flow fields at $x/x_{\mathrm{DDT}} \sim 0.90$ shown in Fig. 5 for both geometries: (i) the topological behavior of the flame is different. The flame surface is larger and has more extensive reaction zone bands approaching near-detonation behavior for the wavy channel, whereas for the fence-type obstacles the flame surface is much larger with many recirculation zones present. This allows enough time for reactions to take place although the conditions for detonation onset may not be fulfilled. (ii) Flame-shock interactions are visible and affect the flame morphology. The propagation regime transition can be observed when the flame reaches speeds on the order of the speed of sound in combustion products. For the cases considered, the calculated speed of sound in bunrt gases is $c_b \sim u/D_{CJ} \sim 0.5$; see table 1 for exact values.
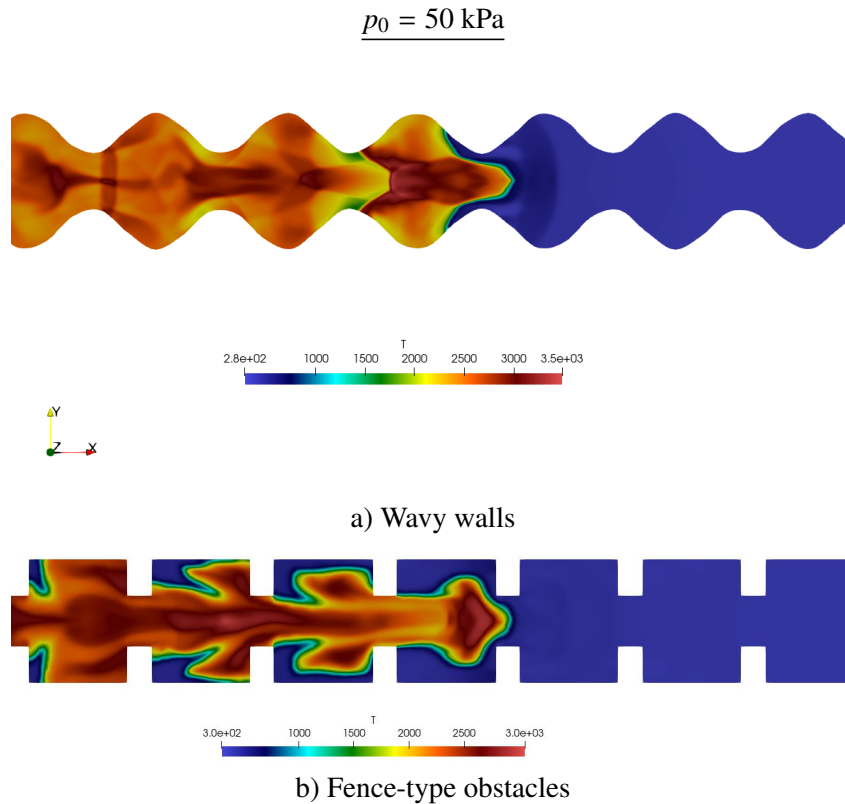
$$p_0 = 50 \text{ kPa}$$

a) Wavy walls

b) Fence-type obstacles

Figure 5: Temperature fields at $x/x_{\mathrm{DDT}} \sim 0.9$ for late stages of FA.

Figure 6 shows the flow fields during steady propagation as the flame-shock complex traverses an obstacle. In the wavy walls case, a *quasi-detonation* regime is established with failure and re-initiation zones, the reaction zone attempts to reach the leading shock ahead, propelled by the explosions of the two shock waves merging into the channel centerline. The flame re-couples with the leading shock supported by the fact that the reaction zone shock-complex is passing through the converging section (compression phase) where it recovers the energy lost during the diverging section (expansion phase). The FT case, on the other hand, displays a different dynamics due to the abrupt area changes: a *quasi-detonation* does not occur, but a regime called *choked flame* or *choking regime* takes place. This fast flame regime can be distinguished from quasi-detonation by a weak lead shock that results in postshock conditions that are not sufficient to cause autoignition of the mixture; see Fig. 6. Unlike the WW case, the FT case is

characterized by an abrupt area change with a small central orifice into which the reaction zone-shock complex is forced to pass; the flow that collides with the vertical walls of the obstacle is thus unable to recover the energy lost during the expansion which prevent the close coupling typical of the flow structure of detonations.

$$p_0 = 50 \text{ kPa}$$

| $t = t_{ref} = 0.799$ ms | $t = t_{ref} + 2\,\mu$s | $t = t_{ref} + 4\,\mu$s | $t = t_{ref} + 6\,\mu$s |

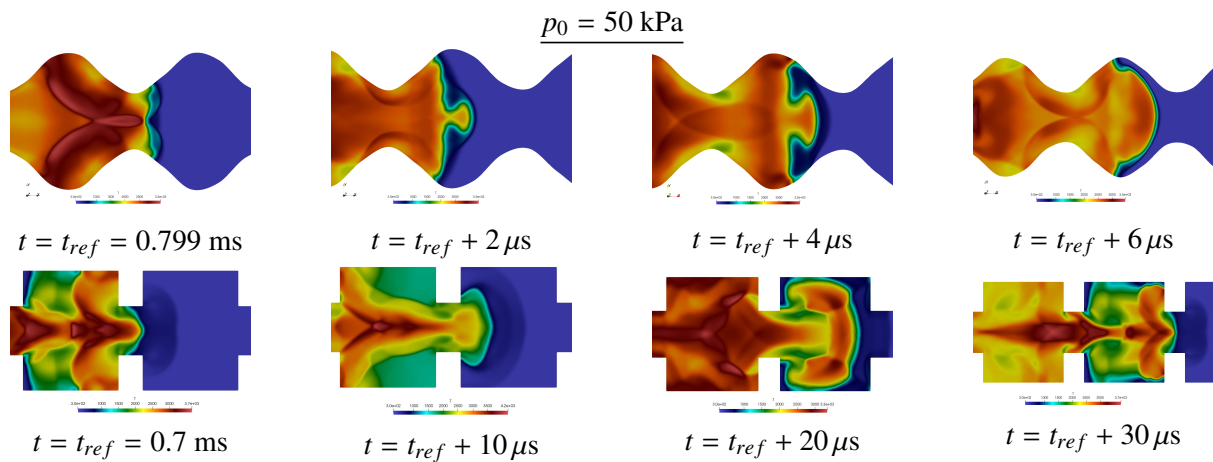| $t = t_{ref} = 0.7$ ms | $t = t_{ref} + 10\,\mu$s | $t = t_{ref} + 20\,\mu$s | $t = t_{ref} + 30\,\mu$s |

Figure 6: Temperature field of flame-shock complex during steady propagation as it traverses an obstacle. Top: *quasi-detonation*. Bottom: *choked flame*. Refer to previous figures for temperature scales.

The soot foils shown in Fig. 7 provide further evidence of the regimes observed. The FT case does not display the characteristic cell formation of detonations [25] whereas for the WW case one cell is present along the height of the channel, in line with the marginal propagation expected for this regime.
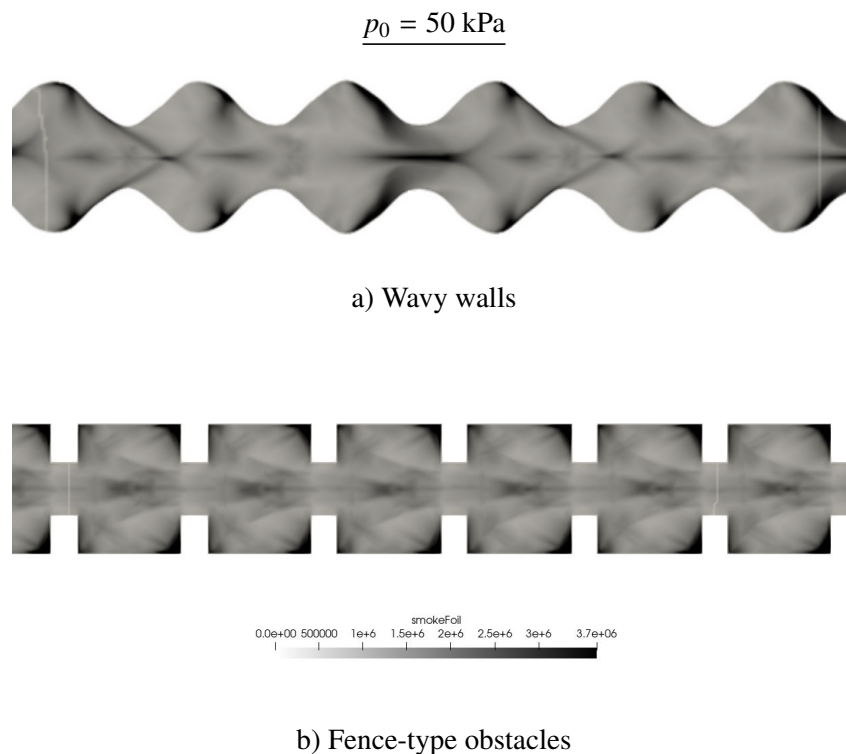
$$p_0 = 50 \text{ kPa}$$

a) Wavy walls

b) Fence-type obstacles

Figure 7: Soot foils during quasi-steady propagation.

10

3.3. On the larger velocity deficit for WW vs FT at 25 kPa

3.3.1. Early/intermediate stages

The flame at 25 kPa starts to propagate through the channel very slowly, generating an initially weak shock wave driven by the chemical combustion process that interacts with the channel geometry. The initial part of the flame evolution is similar to that discussed in section 3.2.1. Expectedly, the pressure decrease to 25 kPa leads to a propagation regime change further downstream the channel; see Fig. 3. Note that in contrast to Fig. 4 in which the early stages of propagtion was described for $p_0 = 50$ kPa, both geometries at $p_0 = 25$ kPa display a comparable volume of unburnt gas upstream the tip of the flame, and a more elongated/thinner topology.
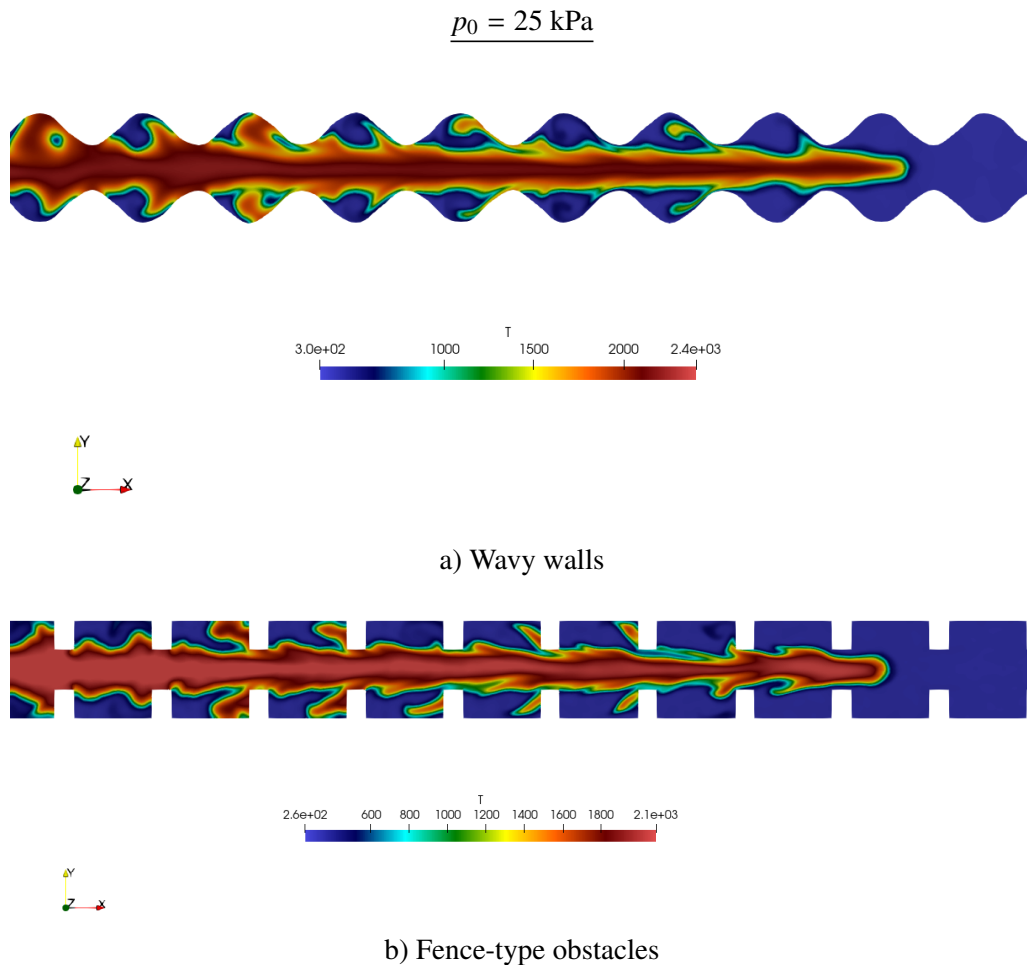
$$\underline{p_0 = 25 \text{ kPa}}$$

a) Wavy walls

b) Fence-type obstacles

Figure 8: Temperature fields at $x/x_{\text{DDT}} \sim 0.5$ for early stages of FA.

3.3.2. Late stages

Both geometries result in the *choked flame* regime at $p_0 = 25$ kPa. This behaviour is verified by the $u - x$ diagram shown in Fig. 2 b) and d) with flame front velocities that asymptote to $u \sim 800$ m/s ($u/D_{CJ} \sim 0.4$). As shown in Fig. 9, the flame brush surface reaches a maximum speed at the flame tip and, as soon as the combustion products flow velocity reaches the local sound speed, the flow behind the flame front is choked; any pressure perturbation generated due to the combustion process cannot reach the flame tip. For the wavy channel, the tip of the flame is further away from the leading shock than

for the fence-type obstacle configuration. The shock waves that collide in the center of the channel in front of the flame create significant losses, such that the flame never reaches the leading shock ahead. Note that in spite of the apparent increased losses due to the abrupt area changes for FT, the flow fields in Fig. 9 display a shorter flame-precursor shock distance, and more numerous recirculation zones and unburnt pockets (i.e., increased flame surface area) leading to steady propagation speeds that are about 10% higher; see Fig. 3. Both geometries yield soot foils similar to that shown in Fig. 7 (b) for 50 kPa in which no cells are formed due to the absence triple points; not included here due to space limitations.

As a final remark, except for the ambiguity obtained at 50 kPa (explained above), the results show that the flame acceleration regimes observed seem to be mostly driven by the ratio of the laminar flame thickness, δ, to a characteristic length defined by the geometry (H or h) since the remaining fundamental combustion properties (i.e., σ and s_L) are essentially constant; see table 1. Choosing the most restrictive length scale, values of $h/\delta \lesssim 10$ should unequivocally lead to *choked flames*. However, when $h \to \delta$ the effect of heat transfer to walls should be accounted for because the propagation dynamics will surely be affected due to an increased likelihood of flame quenching.

$$\underline{p_0 = 25 \text{ kPa}}$$

$$t = t_{ref} = 0.7 \text{ ms}$$

$$t = t_{ref} + 50\,\mu s$$

$$t = t_{ref} + 100\,\mu s$$

$$t = t_{ref} = 2.05 \text{ ms}$$

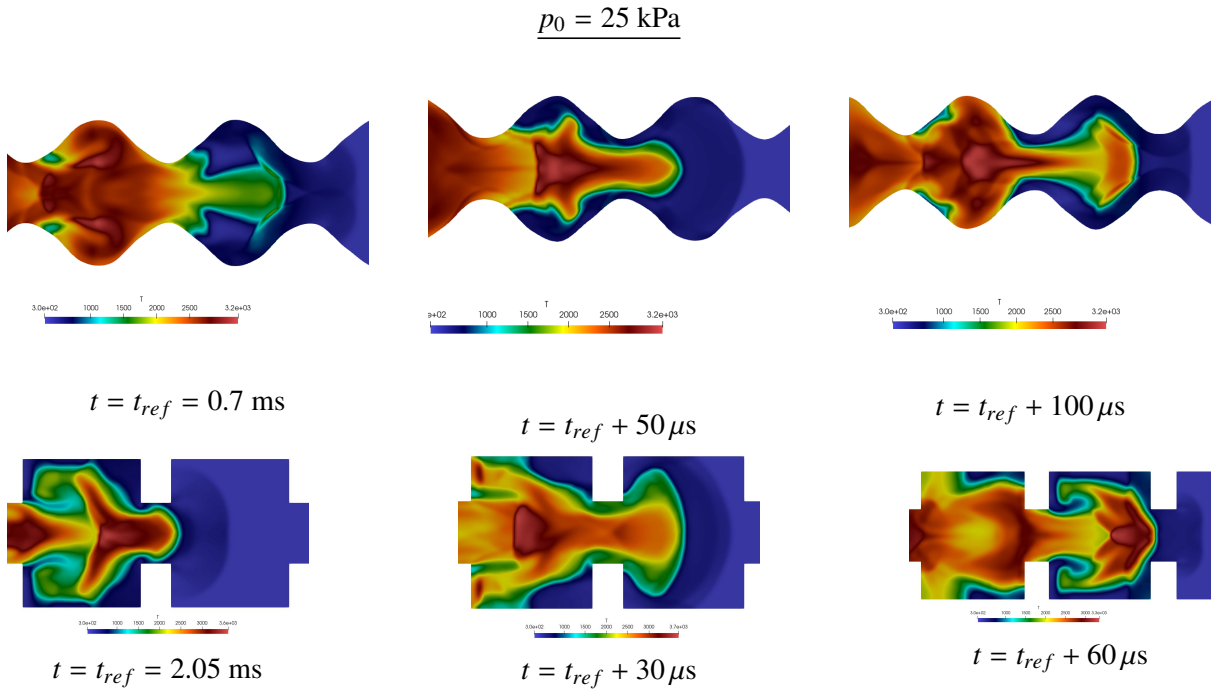$$t = t_{ref} + 30\,\mu s$$

$$t = t_{ref} + 60\,\mu s$$

Figure 9: Temperature field of flame-shock complex during steady propagation, i.e., *choked flame*, as it traverses an obstacle. Refer to previous figures for temperature scales.

4. CONCLUSION

The capabilities of an OpenFOAM solver to reproduce the propagation regimes experimentally observed in obstructed channels were tested. The effect of initial pressure, $p_0 = 25$, 50 and 100 kPa, at constant blockage ratio ($BR = 0.6$) was investigated and compared for channels with wavy walls (WW) and fence-type (FT) obstacles. Results show that for the same initial pressure ($p_0 = 50$ kPa), the obstacle configurations could lead to different final propagation regimes: a *quasi-detonation* for WW, and a *choked-flame* for FT; a non-trivial result suggesting that the combustion regime classification requires the specification of additional parameters. In our case, whether the flame/shock-obstacle interactions are

abrupt (FT) or smooth (WW). At $p_0 = 25$ kPa although both configurations result in *choked flames*, WW seem to exhibit larger velocity deficits than FT due to longer flame-precursor shock distances and the increased presence of unburnt mixture downstream of the tip of the flame that explodes homogeneously providing additional support to the propagation of the flame. Finally, the little variation in fundamental combustion properties and the stark differences in propagation regimes obtained as a function of initial pressure suggests that these may be more fundamentally classified using the ratio of the thermal flame thickness, δ, to a characteristic (smallest) length scale defined by the geometry, h. Future work will assess heat transfer effects on the flame acceleration dynamics by considering channels in which $h \rightarrow \delta$.

ACKNOWLEDGMENTS

REFERENCES

1. Adolfo Iulianelli and Angelo Basile. *Advances in hydrogen production, storage and distribution*. Elsevier, 2014.
2. Paul Amyotte and Fotis Rigasb. Applications of process safety concepts to the hydrogen economy. *Chemical Engineering*, 31, 2013.
3. WC Lattin and Vivek P Utgikar. Transition to hydrogen economy in the united states: A 2006 status report. *International Journal of Hydrogen Energy*, 32(15):3230–3237, 2007.
4. Thierry Poinsot and Denis Veynante. *Theoretical and numerical combustion*. RT Edwards, Inc., 2005.
5. J Melguizo-Gavilanes and R Houim. Experimental and numerical study of flame acceleration and transition to detonation in narrow channels. In *US National Combustion Meeting, College Park, MD*, page 40, 2017.
6. Josué Melguizo-Gavilanes, D Fernández-Galisteo, and A Dejoan. Three-dimensional simulations of lean h2-air flames propagating in a narrow gap: n the validity of the quasi-two-dimensional appoximation. 2021.
7. Said Taileb, Josué Melguizo-Gavilanes, and Ashwin Chinnayya. Influence of the chemical modeling on the quenching limits of gaseous detonation waves confined by an inert layer. *Combustion and Flame*, 218:247–259, 2020.
8. Henry G Weller, Gavin Tabor, Hrvoje Jasak, and Christer Fureby. A tensorial approach to computational continuum mechanics using object-oriented techniques. *Computers in physics*, 12(6):620–631, 1998.
9. Matvey Kraposhin, Arina Bovtrikova, and Sergei Strijhak. Adaptation of kurganov-tadmor numerical scheme for applying in combination with the piso method in numerical simulation of flows in a wide range of mach numbers. *Procedia Computer Science*, 66:43–52, 2015.
10. Alexander Kurganov, Sebastian Noelle, and Guergana Petrova. Semidiscrete central-upwind schemes for hyperbolic conservation laws and hamilton–jacobi equations. *SIAM Journal on Scientific Computing*, 23(3):707–740, 2001.
11. Florian Ettner, Klaus G Vollmer, and Thomas Sattelmayer. Numerical simulation of the deflagration-to-detonation transition in inhomogeneous mixtures. *Journal of Combustion*, 2014, 2014.
12. Yves Ballossier. *Topologies de l'accélération de flammes d'H$_2$-O$_2$-N$_2$ dans des canaux étroits: de l'allumage jusqu'à la détonation*. PhD thesis, ISAE-ENSMA Ecole Nationale Supérieure de Mécanique et d'Aérotechique-Poitiers, 2021.
13. Reza Soleimanpour and Hossain Nemati. Numerical investigation of deflagration to detonation transition in closed ducts under various working conditions. *Acta Astronautica*, 162:109–120, 2019.
14. Ashley M Coates, Donovan L Mathias, and Brian J Cantwell. Numerical investigation of the effect of obstacle shape on deflagration to detonation transition in a hydrogen–air mixture. *Combustion and Flame*, 209:278–290, 2019.
15. G Ciccarelli and S Dorofeev. Flame acceleration and transition to detonation in ducts. *Progress in energy and combustion science*, 34(4):499–550, 2008.
16. Alexander Burcat and Branko Ruscic. Third millenium ideal gas and condensed phase thermochemical database for combustion (with update from active thermochemical tables). Technical report, Argonne National Lab.(ANL), Argonne, IL (United States), 2005.
17. William Sutherland. Lii. the viscosity of gases and molecular force. *The London, Edinburgh, and Dublin Philosophical Magazine and Journal of Science*, 36(223):507–531, 1893.
18. Bruce E Poling, John M Prausnitz, and John P O'connell. *Properties of gases and liquids*. McGraw-Hill Education, 2001.
19. R Mével, S Javoy, F Lafosse, N Chaumeix, G Dupré, and C-E Paillard. Hydrogen–nitrous oxide delay times: Shock tube experimental study and kinetic modelling. *Proceedings of The Combustion Institute*, 32(1):359–366, 2009.

20. Rémy Mével, J Sabard, Junxi Lei, and N Chaumeix. Fundamental combustion properties of oxygen enriched hydrogen/air mixtures relevant to safety analysis: Experimental and simulation study. *international journal of hydrogen energy*, 41(16):6905–6916, 2016.

21. Alexander Kurganov and Eitan Tadmor. New high-resolution central schemes for nonlinear conservation laws and convection–diffusion equations. *Journal of computational physics*, 160(1):241–282, 2000.

22. J Melguizo-Gavilanes, V Rodriguez, P Vidal, and R Zitoun. Dynamics of detonation transmission and propagation in a curved chamber: a numerical and experimental analysis. *Combustion and Flame*, 223:460–473, 2021.

23. David G Goodwin, Harry K Moffat, and Raymond L Speth. Cantera: An object-oriented software toolkit for chemical kinetics, thermodynamics, and transport processes. *Caltech, Pasadena, CA*, 2009.

24. Shannon Browne, J Ziegler, and JE Shepherd. Numerical solution methods for shock and detonation jump conditions. *GALCIT report FM2006*, 6:90, 2008.

25. Joseph E Shepherd. Detonation in gases. *Proceedings of the Combustion Institute*, 32(1):83–98, 2009.